The 19F(α, p)22Ne Reaction at Energies of Astrophysical Relevance by Means of the Trojan Horse Method and Its Implications in AGB Stars

D'Agata, G.; Pizzone, R.G.; La Cognata, M.; Indelicato, I.; Spitaleri, C.; Palmerini, S.; Trippella, O.; Vescovi, D.; Blagus, Saša; Cherubini, S.; ...

CrossMark

The ^{19}F(α, p)^{22}Ne Reaction at Energies of Astrophysical Relevance by Means of the Trojan Horse Method and Its Implications in AGB Stars

G. D'Agata[1,2] , R. G. Pizzone[1] , M. La Cognata[1] , I. Indelicato[1], C. Spitaleri[1,2] , S. Palmerini[3,4], O. Trippella[3,4] , D. Vescovi[3,4] , S. Blagus[5], S. Cherubini[1,2] , P. Figuera[1], L. Grassi[5], G. L. Guardo[1], M. Gulino[1,6] , S. Hayakawa[1,7], R. Kshetri[1,8] , L. Lamia[1,2] , M. Lattuada[1,2] , T. Mijatovic[5], M. Milin[9] , Đ. Miljanic[5,10], L. Prepolec[5], G. G. Rapisarda[1] , S. Romano[1,2], M. L. Sergi[1,2] , N. Skukan[5], N. Soic[5], V. Tokic[5], A. Tumino[1,6] , and M. Uroic[5]

[1] INFN—Laboratori Nazionali del Sud, Via Santa Sofia 62, I-95123, Catania, Italy; g.dagata@lns.infn.it
[2] Dipartimento di Fisica e Astronomia, Università degli Studi di Catania, Via S. Sofia, 64, I-95123, Catania, Italy
[3] Dipartimento di Fisica e Geologia, Università degli Studi di Perugia, via A. Pascoli s/n, I-06123, Perugia, Italy
[4] INFN-sezione di Perugia, via A. Pascoli s/n, I-06123, Perugia, Italy
[5] Ruer Bošković Institute, Bijenicka cesta, 54, 10000, Zagreb, HR, Croatia
[6] Facoltà di Ingegneria ed Architettura, Kore University, Viale delle Olimpiadi, 1, I-94100 Enna, Italy
[7] RIKEN, CNS, 2-1 Hirosawa, Wako, Saitama 351-0198, Japan
[8] Department of Physics, University of Burdwan, Rajbati, Bardhaman—713104, WB, India
[9] Department of Physics, University of Zagreb, Bijenicka 32, Zagreb, Croatia

Abstract

The main source of ^{19}F in the universe has not yet been clearly identified and this issue represents one of the unanswered questions of stellar modeling. This lack of knowledge can be due to the ^{19}F(α, p)^{22}Ne reaction cross-section that has proven to be difficult at low energies: direct measurements stop only at about $\sim$660 keV, leaving roughly half of the astrophysical relevant energy region (from 200 keV to 1.1 MeV) explored only by *R-matrix* calculations. In this work, we applied the Trojan Horse Method to the quasi-free three-body ^{6}Li(^{19}F, p^{22}Ne)d reaction performed at $E_{\text{beam}} = 6$ MeV in order to indirectly study the ^{19}F(α, p)^{22}Ne reaction in the sub-Coulomb energy region. In this way, we obtained the cross-section and the reaction rate in the temperature region of interest for astrophysics and free from electron screening effects. A brief analysis of the impact of the new measured reaction rate in AGB star nucleosynthesis is also presented.

Key words: nuclear reactions, nucleosynthesis, abundances – stars: AGB and post-AGB

1. Introduction

One of the many open questions in astrophysics regards how the nuclear elements are produced and destroyed. Albeit a lot of work has been done in the last few decades, there are still several open issues: one of those concerns fluorine origin. Fluorine is the less abundant element in the region $12 \leqslant A \leqslant 56$ and its only stable isotope, ^{19}F, is one of the few nuclei lighter than ^{56}Fe whose nucleosynthesis is not yet well known (Lugaro et al. 2004). Moreover, the importance of improving our knowledge of the nuclear reaction network for F production and destruction lies in the sensitivity of this element abundance to the physical conditions of nucleosynthesis environments. ^{19}F has been suggested to be produced mainly in three stellar scenarios: Type II supernovae (Woosley & Haxton 1988), Wolf–Rayet stars (Goriely et al. 1989; Meynet & Arnould 2000; Palacios et al. 2005), and asymptotic giant branch (hereafter, AGB) stars (Forestini et al. 1992). Moreover, white dwarf merging was also suggested as a possible site of ^{19}F production (Longland et al. 2011). Among these, AGB stars have been proven to be sites of ^{19}F production through observations of molecular and atomic lines at the 2.3 μm in the spectra of C-stars (Jorissen et al. 1992; Abia et al. 2009, 2010; Alves-Brito et al. 2011) and of metal-poor objects (Schuler et al. 2007; Lucatello et al. 2011). However, it is not clear whether those stars might produce enough fluorine to account for its galactic abundance. In particular, the hypothesis that AGB stars might be the main source of fluorine in the solar neighborhood

is still a matter of debate (Kobayashi et al. 2011; Jönsson et al. 2014; Abia et al. 2015; Pilachowski & Pace 2015). Very recently, the trends of [F/Fe] versus [Fe/H] and [F/O] versus [O/H] abundances observed in a sample of 49 K giants by Jönsson et al. (2017) seem to definitively exclude a significant contribution from type-II supernovae (SNII) to the amount of fluorine in the solar neighborhood. This fact hints that AGB and eventually Wolf–Rayet stars are the main sites of ^{19}F production.

According to the commonly accepted models, AGB stars are composed of a degenerate C–O core, surrounded by a He-shell, a H-shell, and an extended convective envelope. The radiative burning of the He-shell is periodically interrupted by convective instabilities, called thermal pulses (hereafter TP), due to the on-set rapid activation of the He-burning. At the end of each TP, the convective envelope penetrates into the inner radiative layers down to the He-rich region; this episode, called third dredge-up (TDU), results in an enrichment of the stellar envelope with fresh products of the nucleosynthesis and in a consequent penetration of proton-rich material in the He-rich region. When the H-shell reactivates, the temperatures of the region below reaches values high enough that injected protons might be captured by ^{12}C producing ^{13}C and ^{14}N. While the ^{13}C is, via the ^{13}C(α, n)^{16}O and together with ^{22}Ne, the main source of neutron for the *s*-process in AGB stars, ^{14}N leads to the production of ^{19}F, by means of the chain ^{14}N(n, p)^{14}C(α, γ)^{18}O(p, α)^{15}N(α, γ)^{19}F (Cristallo et al. 2014, and references therein). Nitrogen is therefore considered to be a neutron "poison," but it is strongly tied to ^{19}F production. On the other hand, fluorine is destroyed in stellar interiors by proton, neutron, and α-capture reactions. As a consequence, fluorine

---
[10] Deceased.

abundance can provide crucial information in order to constrain the physical conditions of the stellar interior. Recent studies (Lugaro et al. 2004; Cristallo et al. 2014) have shown that the $^{19}\text{F}(\alpha, \text{p})^{22}\text{Ne}$ reaction is the ^{19}F destruction channel with the largest effect on fluorine nucleosynthesis.

This work presents new experimental results about one of the main channels for the ^{19}F destruction: the cross-section of the $^{19}\text{F}(\alpha, \text{p})^{22}\text{Ne}$ reaction is measured for the first time in the energy range typical of stellar nucleosynthesis.

2. State-of-the-art and Theoretical Framework

As introduced in the previous section, the chain of reactions for the ^{19}F production is quite well known, but some uncertainties on its destruction still remain; in AGB stars, fluorine can be processed via the $^{19}\text{F}(\text{p}, \alpha)^{16}\text{O}$ or the $^{19}\text{F}(\alpha, \text{p})^{22}\text{Ne}$ reactions. Which reaction channel prevails on the other depends on the temperature and on hydrogen and helium abundance of the stellar environment (Lugaro et al. 2004; Cristallo et al. 2014). Another way to destroy fluorine is $^{19}\text{F}(\text{n}, \gamma)^{20}\text{F}$, triggered by the neutrons from $^{13}\text{C}(\alpha, \text{n})^{16}\text{O}$ and $^{22}\text{Ne}(\alpha, \text{n})^{25}\text{Mg}$.

As already mentioned, the reaction rate for $^{19}\text{F}(\alpha, \text{p})^{22}\text{Ne}$ is characterized by large uncertainties in the energy range corresponding to the typical temperatures of stellar He-burning. The lowest energy at which the $^{19}\text{F}(\alpha, \text{p})^{22}\text{Ne}$ reaction was measured corresponds to ∼660 keV (Ugalde et al. 2008), leaving almost half of the Gamow region still uncovered in the center-of-mass system: at the He-burning stage, in fact, the relevant Gamow window goes from 200 keV to 1.1 MeV. This energy range is also really hard to explore using direct measurements due to the Coulomb barrier effects, which for $^{19}\text{F} + \alpha$ is about 3.1 MeV.

Because of the lack of experimental data, a simplified expression of the rate computed by Caughlan & Fowler (1988) is still largely employed in several nucleosynthesis codes. The Caughlan's estimate (Caughlan & Fowler 1988) is based on an optical model to calculate the cross-section of compound nuclear reactions with overlapping resonances and the resulting reaction rate is in reasonable agreement with Hauser–Feshbach calculations (Thielemann et al. 1986). In Ugalde et al. (2008), the cross-section measured in the energy range $E_{\text{C.M.}} = 0.66 \div 1.6$ MeV was computed with an *R-matrix* fit and the reaction rate for astrophysical application was determined for $E_{\text{C.M.}} \geqslant 0.66$ keV, while the cross-section and the $S(E)$-factor were extrapolated at lower energies. Nevertheless, the reduced γ_α width of the involved resonances was roughly estimated (Ugalde et al. 2008) and a more precise experimental determination is needed in the Gamow energy range to better understand fluorine nucleosynthesis. Nuclear reactions at energies below the Coulomb barrier (which is usually on the order of some MeV) have proven to be really difficult. For this reason, the reactions of astrophysical interest, occurring in the energy range between some keV and a few MeV are really challenging. Coulomb barrier effects, in fact, strongly reduce the cross-section (to the order of some picobarn or even lower). A way to overcome such difficulties is to extrapolate the measured cross-sections down to the "unknown" region. This procedure nevertheless is dangerous, and can be strongly affected by the presence of unknown resonances. In this energy range, the electron screening (Assenbaum et al. 1987) can also falsify the measurement, due to the fact that in the laboratory the target particle is surrounded by electrons, thus reducing the effective Coulomb barrier. For all of these reasons, many
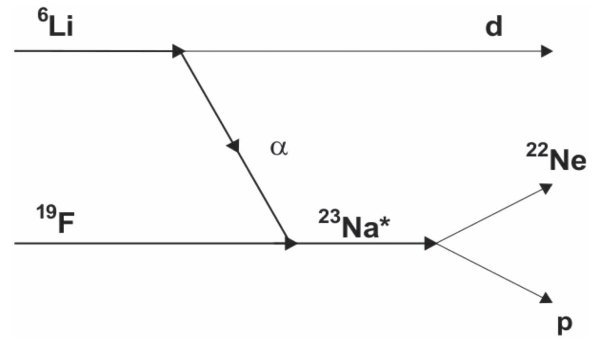

Figure 1. Sketch of the quasi-free process discussed in the text. The upper pole represents the ^6Li break-up, while the lower one shows the binary interaction of astrophysical interest $^{19}\text{F}(\alpha, \text{p})^{22}\text{Ne}$.

indirect methods have been proposed over the years (Tribble et al. 2014, and references therein), and among these the Trojan Horse Method (hereafter THM; Spitaleri et al. 1991) has proven to be really useful to study reactions between charged particles at low energies. Using this method, a lot of very important reactions in Big Bang nucleosynthesis (Tumino et al. 2011; Pizzone et al. 2014; Tumino et al. 2014), light element depletion (Lamia et al. 2013), and AGB nucleosynthesis (Palmerini et al. 2013; La Cognata et al. 2015) were studied. Concerning the last scenario, THM was also used to study the $^{19}\text{F}(\text{p}, \alpha)^{16}\text{O}$ (Indelicato et al. 2017). The THM can also be used in reactions with unstable nuclei like $^{18}\text{F}(\text{p}, \alpha)^{15}\text{O}$ (Cherubini et al. 2015; Pizzone et al. 2016) and neutrons in the entrance channel (Gulino et al. 2013).

The aim of THM is to study a two-body reaction, in our case $^{19}\text{F}(\alpha, \text{p})^{22}\text{Ne}$, by means of a suitable three-body one in the exit channel. The chosen reaction for this work is the $^{19}\text{F}(^6\text{Li}, \text{p}^{22}\text{Ne})d$ (Figure 1), because of the well-known cluster structure of the ^6Li particle, that can be considered as composed by $\alpha \oplus d$. For the present case, under proper kinematical conditions (Spitaleri et al. 2001) the deuteron particle can be considered as a spectator for the two-body process $^{19}\text{F}(\alpha, \text{p})^{22}\text{Ne}$. In this theoretical framework, if the process is a Quasi-free (hereafter QF) one, the participant nucleus (α particle), can induce the reaction right inside the Coulomb field, without barrier and electron screening effects. Using the *Modified R-matrix* formalism (Mukhamedzhanov et al. 2008; La Cognata et al. 2011; Tribble et al. 2014), which is necessary due to the presence of resonant levels of ^{23}Na, the two-body half-off-energy shell (hereafter HOES) differential cross-section can be written as a function of the overlapping function $I_{\text{F}\tau}^{\text{Na}} = \langle \Phi_\tau | \phi_{\text{F}} \rangle$ of the internal wave-function of the ^{23}Na system, excited to a certain level τ, and of the bound-state wave-function of ^{19}F. This situation can be expressed as a parameterization (with an arbitrary boundary condition) of the entrance channel $\alpha + ^{19}\text{F}$ and of the reduced width amplitude $\gamma_{\alpha^{19}\text{F}}$, where the last term represents the *R-matrix* amplitude for the two-body resonant reaction (proceeding through several ^{23}Na bound states τ into a certain final state c', corresponding to excited states of ^{22}Ne). The $\gamma_{\alpha^{19}\text{F}}$ are all observable reduced widths: in our case, we use a one-level, multichannel approach. Therefore, only one boundary condition is needed and the Thomas approximation can be used. If there is no interference between resonances, the TH cross-section can be calculated, in

plane-wave, as follows:

$$\frac{d^2\sigma_{\alpha+\,^{19}\mathrm{F}\to c'}}{dE_{\alpha^{19}\mathrm{F}}\,d\Omega_d} = NF\sum_\tau (2J_\tau+1)\left|\sqrt{\frac{k_{c'}(E_{\alpha^{19}\mathrm{F}})}{\mu_{c'}}}\right.$$

$$\left.\times\left|\frac{\sqrt{2P_l(k_{c'}R_{c'})}\,M_\tau(p_{\alpha^{19}F}R_{\alpha^{19}F})\gamma_{c'}\,\gamma^\tau_{\alpha^{19}\mathrm{F}}}{D_\tau(E_{\alpha^{19}\mathrm{F}})}\right|\right|. \qquad (1)$$

Equation (1) shows the strongest advantage of THM measurements with respect to the direct one. As shown in Tribble et al. (2014), the presence of the factor $P_l^{1/2}(k, R)$ compensates for the Coulomb and centrifugal barrier penetration factor of the entrance channel. This method is therefore able to reach really low energies (even zero). Here NF is a normalization factor, J_τ is the spin of the τth resonance, $k_{c'}$ is a kinematical factor equal to $k_{c'}(E_{\alpha^{19}\mathrm{F}}) = \sqrt{2\mu_{c'}(E_{\alpha^{19}\mathrm{F}} + Q)}\big/\hbar$ (where Q is the Q-value for the reaction and $E_{\alpha^{19}\mathrm{F}}$ represents the relative energy of the two interacting particles), P_l is the penetration factor (in lth wave), and $R_{c'}$ and $R_{\alpha^{19}\mathrm{F}}$ are the channel radii. The last remaining term, $M_\tau(p_{\alpha^{19}\mathrm{F}}R_{\alpha^{19}\mathrm{F}})$, can be written as follows:

$$M_\tau(p_{\alpha^{19}\mathrm{F}}R_{\alpha^{19}\mathrm{F}})$$
$$=\left[(B_{\alpha^{19}\mathrm{F}}-1)\,j_{l_\tau}(\rho) - \rho\frac{\partial j_{l_\tau}(\rho)}{\partial\rho}\right]_{\rho=p_{\alpha^{19}\mathrm{F}}R_{\alpha^{19}\mathrm{F}}}. \qquad (2)$$

In Equation (2), $B_{\alpha^{19}\mathrm{F}}$ is an arbitrary boundary condition that is used to yield the observed resonance parameters, $j_{l_\tau}(\rho)$ is the spherical Bessel function, and $p_{\alpha^{19}\mathrm{F}} = \sqrt{2\mu_{\alpha^{19}\mathrm{F}}(E_{\alpha^{19}\mathrm{F}} + B_{\alpha d})}\big/\hbar$, where $B_{\alpha d}$ is the binding energy of the cluster $^6\mathrm{Li} = \alpha\oplus\mathrm{d}$. Finally, the denominator of Equation (1), D_τ, is the usual R-matrix one for the one-level multichannel formula (Lane & Thomas 1958; La Cognata et al. 2011)

$$D_\tau(E_{\alpha^{19}\mathrm{F}}) = E_\tau - E_{\alpha^{19}\mathrm{F}}$$
$$-\sum_c(\gamma^\tau_c)^2(S_c - B_c) - I\sum_c 2P_c(\gamma^\tau_c)^2, \qquad (3)$$

where S_c is the shift function for channel c, which is one of the possible open channels. Equation (1) is a simplified version of the one given in the literature (Tribble et al. 2014; Mukhamedzhanov et al. 2017), which is the formally correct one. This simplification can be done since the differences between the two can be considered negligible if compared with the experimental errors, as discussed in several works (see La Cognata et al. 2010 and La Cognata et al. 2011 for further details).

In the following analysis, the Coulomb interaction between $^{22}\mathrm{Ne}$ and d was not taken into account. We used the plane-wave approximation, following Dolinsky et al. (1973). This seminal work, on which the formalism above is based, proved that the plane-wave approximation can supply an accurate energy dependence of the three-body cross-section, but in a much simpler way than the distorted-wave approximation.

3. The Experiment

The $^6\mathrm{Li}(^{19}\mathrm{F}, \mathrm{p}^{22}\mathrm{Ne})\mathrm{d}$ experiment was performed at the Ruer Bošković Institute (Zagreb, Croatia) using a 6 MeV $^6\mathrm{Li}$ beam impinging on a 150 μg cm^{-2} $^7\mathrm{LiF}$ target.

The detection apparatus (reported in Figure 2) was composed of two $\Delta E - E$ telescopes, each of them made up by the thin silicon detector (15 μm and 9 μm thick, respectively) and a
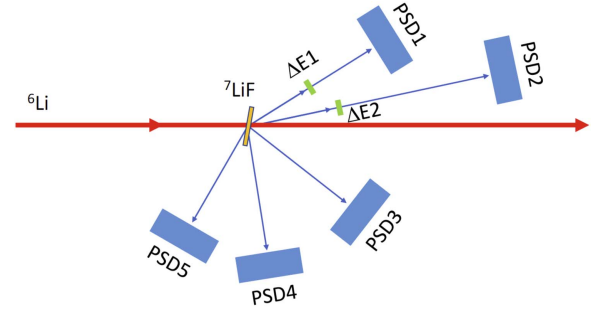

Figure 2. Sketch of the adopted experimental setup. The two $\Delta E - E$ telescopes are situated on one side of the beam axis. Three PSDs were placed on the other side with respect to the beam direction.

Table 1
Experimental Features of the Setup Described in the Text

Det.	Distance [cm]	Angle [deg]	Range [deg]	$\Delta\Omega$[mSr]
PSD1	17.6	32.3	±7.2	16
PSD2	20.6	12.3	±6.6	12
PSD3	10.3	−37.7	±12.4	47
PSD4	10.3	−81.0	±9.2	47
PSD5	9.1	−119.9	±11.0	6
$\Delta E1$	6.0	32.3	±9.6	89
$\Delta E2$	7.5	12.3	±7.7	57

thick position sensitive detector (PSD, 500 μm thick), placed as reported in Table 1.

PSD1 and 2 were devoted to deuteron detection, while PSD3, PSD4, and PSD5 to protons. ΔE stages, having a 81.7 mm^2 active surface, are placed with the same central angle as PSD1 and PSD2. Equally spaced grids, placed in front of each PSD, were used for angular calibration. In this experiment, it was preferred to detected the spectator particle instead of the heavy fragment, $^{22}\mathrm{Ne}$, because of the emission angles and the energy loss for this particle: from simulations, it turns out to be emitted at forward angles ($0° \leqslant \vartheta_{^{22}\mathrm{Ne}} \leqslant 6°$), where a large contribution from the pure elastic scattering of $^6\mathrm{Li}$ on $^{19}\mathrm{F}$ is expected, and with a maximum energy (of about 3.5 MeV) that would make it virtually impossible to detect due to both energy loss and angular straggling in the solid target. Moreover, using these kinds of thin silicon detectors for particle discrimination is impossible in this case, since the $^{22}\mathrm{Ne}$ particle would need at least 11 MeV to pass through the ones used in this experiment, and ionization chambers would be too bulky to be installed at the chosen angles.

The average beam intensity for this experiment was around 5 enA, leading to an elastic scattering rate on PSD2 of about 4 kHz for the $^6\mathrm{Li}+^{19}\mathrm{F}$ interaction. For this reason, a 15 μm thick piece of aluminum foil was placed in front of PSD2.

The $^7\mathrm{LiF}$ target is then tilted at 10° with respect to the beam direction, in order to maximize statistics for PSD1 and PSD2, avoiding shadowing from the target frame at the same time. This expedient, in fact, reduces the volume of the target traversed by the outgoing deuterium particles, minimizing energy loss. This has proven to be crucial because of the low reaction rate expected for the $^{19}\mathrm{F}(\alpha, \mathrm{p})^{22}\mathrm{Ne}$ and the low energy of the outgoing deuteron nuclei (5 MeV maximum) determined by means of a proper Monte Carlo simulation.

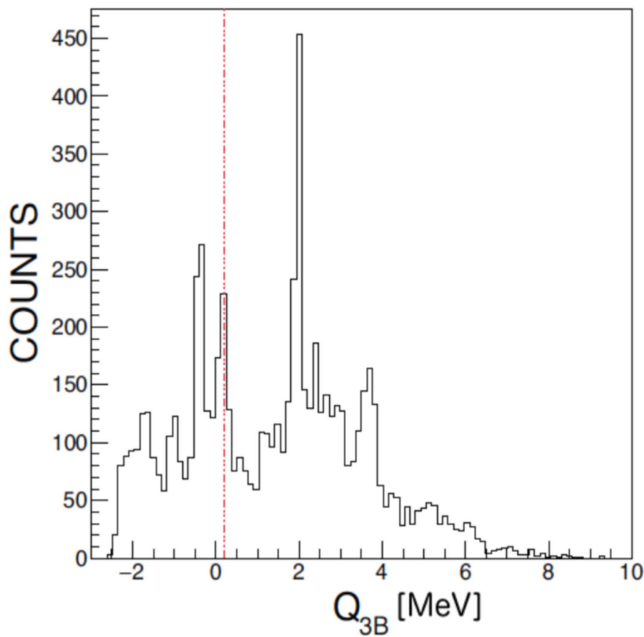The trigger of the acquisition system was made by coincidences between any combination of two detectors placed

Figure 3. Total Q_{3B} clearly shows the presence of many different reactions, but a structure peaked among the theoretic value for the ^{6}Li(^{19}F, p^{22}Ne)d at $Q_{3B} \simeq 0.2$ MeV is also evident (red dashed line). The other evident peak at ~ 2 MeV is due to the two-body reaction ^{6}Li(^{7}Li, t)^{10}B triggered by the ^{7}Li present in the target and the one at approximately -0.4 MeV can be due to the first excited state of the ^{23}Na compound nucleus.

at the opposite sides of the beam. A 250 ns coincidence window was set to reduce spurious coincidence contribution. The angular resolution of each PSD turned out to be around $0°.25$; the precise determination of the angle of emission is crucial for such measurements, because it allows us to reconstruct the kinematic variables involved in the process (i.e., relative energies and center-of-mass energy). Detectors were calibrated by means of standard α-sources and proton scattering on Au and CD$_2$ targets at different energies. The energy resolution for PSDs was around 0.8%, in agreement with the data sheet for the PSD detectors. Taking into account the beam spot size (which was minimized to a 1 mm radius), and the straggling of both beam and emitted particles into the target, the final energy resolution was evaluated to be around 1% for PSD3. In the case of PSD2, the particles emerging from the target must pass by the ΔE stage (the thin silicon detector) and the thin aluminum absorber. For this reason, the energy resolution for PSD2 is at about 3%.

4. Data Analysis

After the calibration stage, the $\Delta E - E$ telescopes were used to select deuterons (spectator particle) coming from the three-body reaction, along with protons detected by the PSDs.

As can be seen in the three-body Q-value spectrum, there are a lot of peaks in addition to the one we are looking for (Figure 3), corresponding to a three-body Q-value equal to $Q_{3B} = 0.2$ MeV for the ^{6}Li(^{19}F, p^{22}Ne)d reaction. There is evidence that the three-body reaction of interest is taking place, but the data require further reduction. For this reason, we decided to plot the three-body Q_{3B} versus the detection angle for PSD2 and PSD3.

In this way, we obtain what is shown in Figure 4: if the reaction of interest is taking place, experimental data must gather around a straight line corresponding to the expected Q_{3B}

value. This procedure is also proof that the calibration is good, due to the fact that Q_{3B} seems to be independent of the angle of detection of the particles. Using the data selection reported in Figure 4, where a clustering among the red line corresponding to $Q_{3B} \approx 0.2$ MeV is evident, and taking into account the spectra arising from the Time Amplitude Converter (TAC) module (where particles coming from different reactions can be separated due to different times of emission), we are able to select the contribution coming from the ^{6}Li(^{19}F, p^{22}Ne)d channel.

In Figure 5, the Q-value for the selections reported above is shown, and a clear peak connected to the reaction of interest whose centroid is in agreement with the theoretically predicted value (red vertical line), $Q_{\text{theor}} \simeq 0.2$ MeV, can be seen. Data are then studied and selected in order to check for the presence of QF processes.

This step is of great importance, as THM can be applied to QF events only. In particular, the p + d + ^{22}Ne channel could come from three different sequential decays, such as:

1. ^{6}Li + ^{19}F $\rightarrow$ ^{23}Na* + d $\rightarrow$ ^{22}Ne + p + d;
2. ^{6}Li + ^{19}F $\rightarrow$ ^{3}He* + ^{22}Ne $\rightarrow$ ^{22}Ne + p + d;
3. ^{6}Li + ^{19}F $\rightarrow$ ^{24}Na* + p $\rightarrow$ ^{22}Ne + p + d.

While the first reaction chain leads to the final channel via ^{23}Na* excited states, the other ones show intermediate states that were involved, which consequently cannot play the role of spectators. If one of these possible two-step reactions is taking place, their presence would be ascertained looking at relative energies of 2D spectra. Following the procedure explained in previous works (see Spitaleri et al. 2004, and references therein), there is no evidence of the presence of ^{3}He and ^{24}Na excited states, while a strong level coming from ^{23}Na can be detected for $E_{^{22}\text{Ne}-p} \approx 0.4$ MeV. This level does not interfere with our data due to the fact that it lies at higher p_s values ($p_s \geqslant 60$ MeV/c^2) that are above the range of interest: sequential processes are therefore not present in the selected data. The presence of QF processes is then ascertained by studying the momentum distribution of the spectator particle: if the process is a QF one, then the momentum distribution must follow a certain trend. In our case, the momentum distribution behavior of the deuteron particle inside ^{6}Li is given by the Hänckel function (see Barbarino et al. 1980 for details).

Following the THM prescriptions, one can obtain the momentum distribution $|\Phi(p_s)|^2$ by dividing the triple differential cross-section for a kinematic factor after selecting a center-of-mass energy and angular range where the two-body HOES cross-section is roughly constant (see Pizzone et al. 2005 for further discussion).

The result is reported in Figure 6 as solid black circles: our data trend is consistent with the expected momentum distribution of a deuteron cluster inside ^{6}Li (green curve in Figure 6). The full width at half maximum (FWHM) value of the momentum distribution is equal to 53 MeV/c $\pm$ 7 MeV/c. The minimum absolute value of the momentum in this case does not reach zero like in most of the THM applications, and this is due to the fact that we detected the spectator particle (whose momentum distribution is reconstructed in most cases) and that the TH nucleus is in the beam. This distribution should show its maximum at $|p_s| = 0$, corresponding to a detection angle around zero degrees in the laboratory system, which cannot be reached with the present experimental setup.
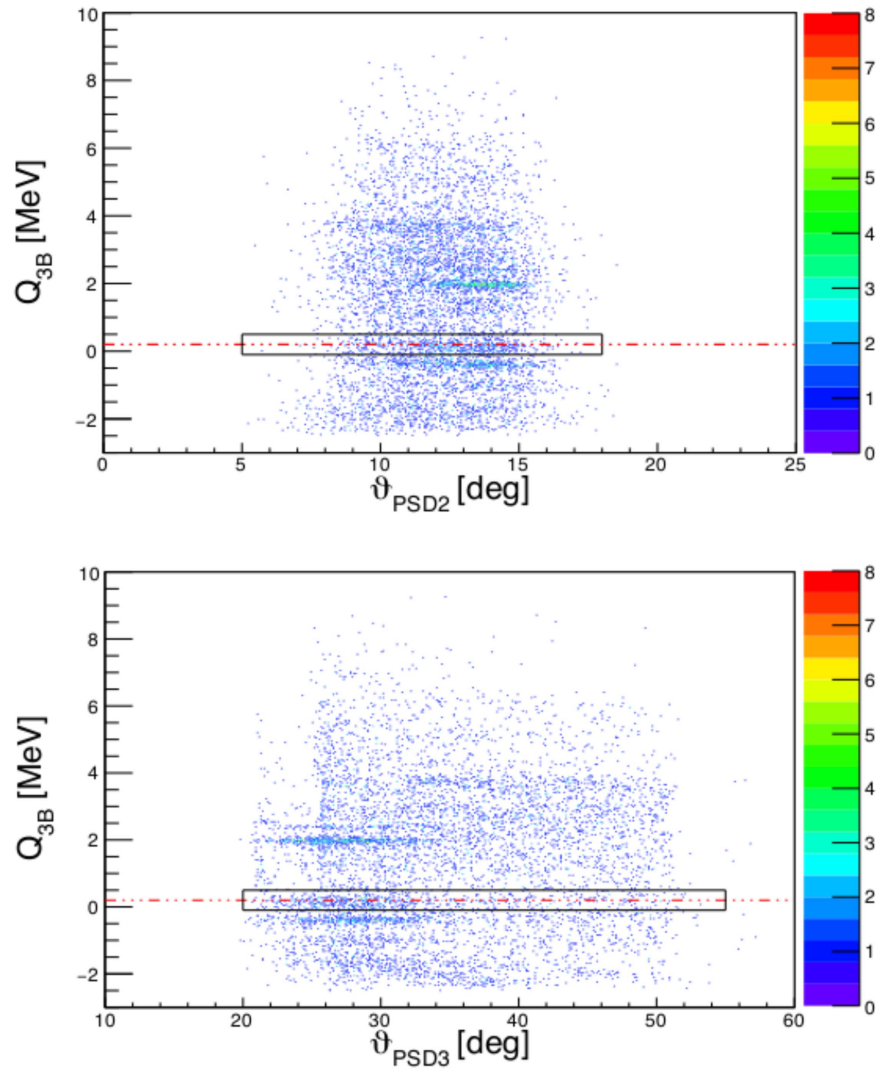
Figure 4. Three-body Q-value (Q_{3B}) vs. angular position for PSD2 (upper panel) and PSD3 (lower panel; see the text for details). The black boxes represent the selected events adopted in the following analysis.
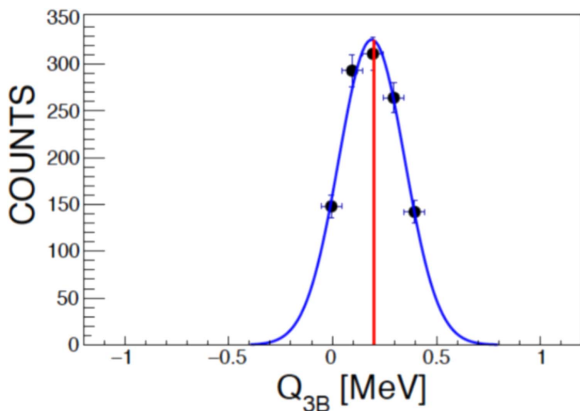

Figure 5. Q-value spectrum for the ^{6}Li(^{19}F, p^{22}Ne)d reaction. A Gaussian fit to the experimental data is also reported with the blue line, while the red one shows the position of the theoretical Q-value. Errors along the y-axis represent the statistical error, while those along the x-axis are calculated by means of standard error propagation, considering the errors on energy and angle measurement of PSDs.

The blue curve in Figure 6 is the theoretical prediction of the spectator momentum distribution obtained using the Woods–Saxon potential with the standard geometrical parameters (see

Pizzone et al. 2009). Hereafter, only events with $p_s \leqslant$ 50 MeV/c will be considered.

The transferred momentum is calculated as $\mathbf{q}_t = \mathbf{p}_{\text{Li}} - \frac{\mathbf{p}_p + \mathbf{p}_{\text{Ne}}}{2}$, and for the present case its module is equal to $\sim$200 MeV/c. In Figure 7, the blue solid circle represents the value of FWHM of the momentum distribution, obtained in this experiment as a function of q_t. The black diamonds refer to other results for ^{6}Li break-up at various energies reported in Pizzone et al. (2005). The fact that the FWHM of Figure 6 is consistent, as a function of the transferred momentum, with the trend already present in the literature hints at the presence and separability of the QF process from all the others, which may feed the three-body reaction and also allows us to take into account the distortion effects in the momentum distribution for lower transferred momentum, as described in Pizzone et al. (2005).

5. Results

The three-body reaction yield is plotted as a function of $E_{\text{C.M.}}$ in Figure 8 (upper panel), being

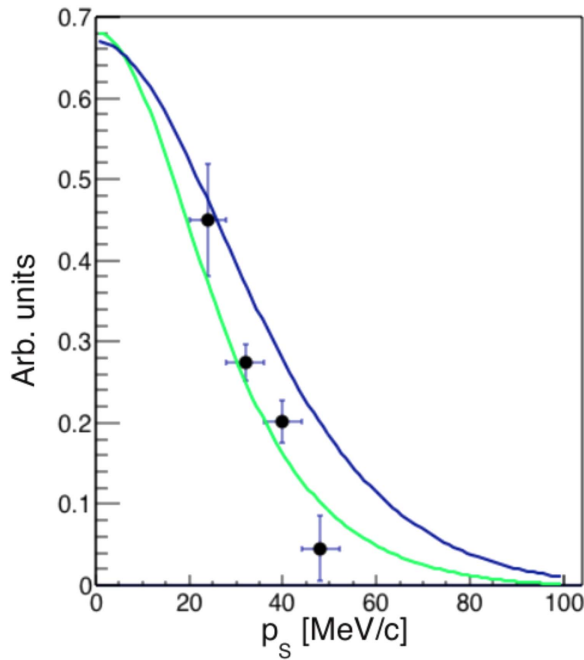$$E_{\text{C.M.}} = E_{p-^{22}\text{Ne}} - Q_{2B}, \quad (4)$$

Figure 6. Experimental momentum distribution for deuteron and alpha in ^{6}Li as a function of their relative momentum (solid circles). The fit is made with a Hänkel function (green line) and compared with theoretical calculations (blue line; see Pizzone et al. 2009). Errors are calculated as in Figure 5.
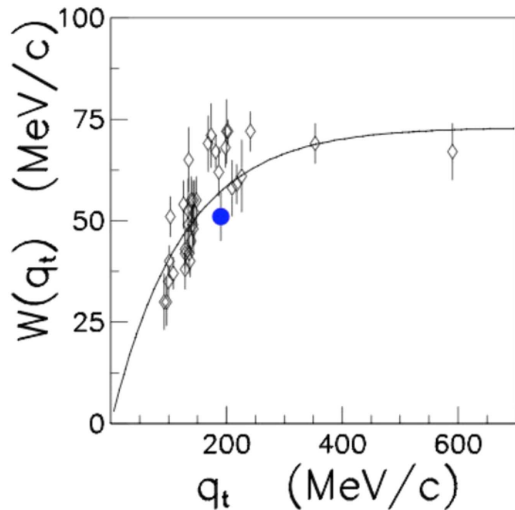

Figure 7. FWHM of the momentum distribution for deuteron inside ^{6}Li as a function of q_t, which is the momentum transferred from ^{6}Li to the deuteron. The blue circle represents the value obtained in this experiment, while the diamonds represent values from the literature (Pizzone et al. 2005).

Figure 8. Three-body reaction yield for the ^{19}F(α, p)^{22}Ne reaction (upper panel) as a function of $E_{\text{C.M.}}$ and the product of the kinematic factor times the momentum distribution of the $\alpha - d$ relative motion inside ^{6}Li (lower panel).

Table 2
Characteristics of the ^{23}Na States Included in the Present Analysis

E_R [MeV]	$E_{\text{C.M.}}$ [MeV]	J^π	γ_α [MeV$^{1/2}$]	γ_p [MeV$^{1/2}$]	$\gamma_{p'}$ [MeV$^{1/2}$]
10.477	0.01	$3/2^+$	$0.0010^{+0.0001}_{-0.0002}$	0.124	0.342
10.616	0.149	$5/2^+$	$0.0055^{+0.0002}_{-0.0080}$	0.087	0.327
10.823	0.356	$3/2^+$	$0.0070^{+0.0001}_{-0.0010}$	0.131	0.417
10.907	0.44	$5/2^+$	$0.0007^{+0.0001}_{-0.0002}$	0.054	0.350
10.972	0.505	$5/2^+$	$0.0090^{+0.0002}_{-0.0009}$	0.044	0.184
10.994	0.527	$3/2^+$	$0.0050^{+0.0002}_{-0.0010}$	0.011	0.079
11.038	0.571	$3/2^+$	$0.0027^{+0.0002}_{-0.0005}$	0.049	0.179
11.109	0.642	$5/2^+$	$0.0120^{+0.0015}_{-0.0015}$	0.016	0.096
11.273	0.806	$3/2^+$	0.003*	0.045	0.279
11.280	0.812	$3/2^+$	0.003*	0.127	0.320
11.303	0.836	$3/2^+$	0.003*	0.105	0.148

Note. The measured central values, the J^π of the levels, and the reduced widths involved in the *R-matrix* fit calculations discussed in Pizzone et al. (2017) are also reported. Values marked with asterisks are taken from Ugalde et al. (2008).

with the first term representing the relative energy of the ejectiles and Q_{2B} the Q-value of the ^{19}F(α, p)^{22}Ne two-body reaction, following the post-collision prescriptions. The reported uncertainties are due to the statistical error. The HOES cross-section for the binary ^{19}F(α, p)^{22}Ne reaction is extracted, following Equation (1) and using the approach described in Pizzone et al. (2017), after dividing the measured triple differential cross-section by the product of the kinematic factor and the momentum distribution of the $\alpha - d$ relative motion inside ^{6}Li (see the lower panel of Figure 8).
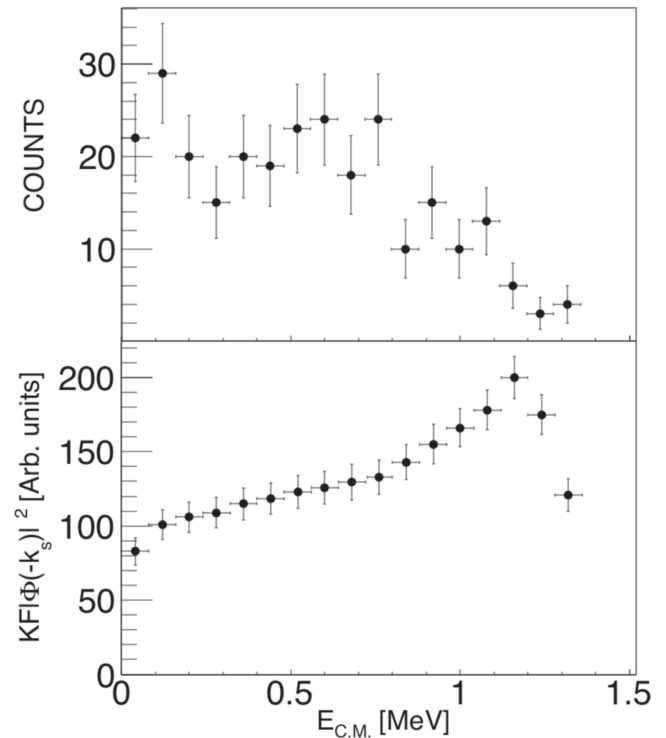
The experimental data show a trend that is the convolution of several states in the ^{23}Na compound nucleus, which are reported in Table 2.

Then we proceeded with the analysis of the HOES cross-section in the *Modified R-matrix* approach (Pizzone et al. 2017), to deduce the reduced widths and correct for HOES effects and energy resolution. A weighted fit of the cross-section in arbitrary units is performed by means of the one-level, three-channel *Modified R-matrix* formula (Pizzone et al. 2017), assuming $l = 2$ in the calculations. This choice is made taking into account the γ_α values measured by Ugalde et al.

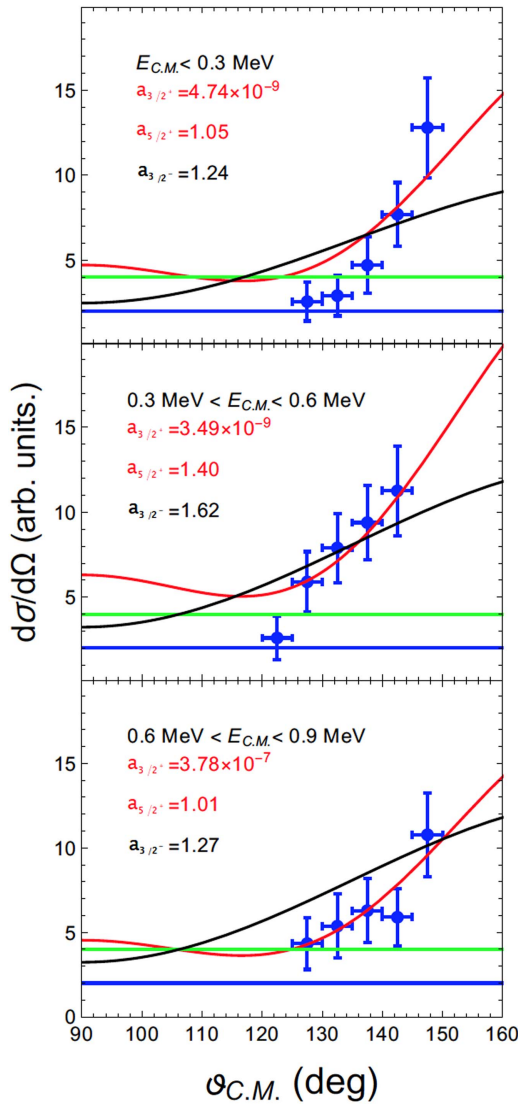**Figure 9.** Experimental angular distribution for the $^{19}F(\alpha, p)^{22}Ne$ reaction ($\frac{d\sigma}{d\Omega}$ vs. $\vartheta_{C.M}$, where $\vartheta_{C.M}$ is the emission angle of the proton in the center-of-mass reference frame of the reaction). The blue solid circles are the present experimental data. The red line represents a fit to the experimental data done by means of a linear combination of $J^\pi = 3/2^+$ and $J^\pi = 5/2^+$ angular distributions, using the equations given in Blatt & Biedenharn (1952) and La Cognata et al. (2015). The black, green, and blue lines are instead angular distributions for J^π equal to $3/2^-$ (with $a_{3/2^-}$ as normalization coefficient), $1/2^+$, and $1/2^-$ (multiplied by a factor of two to separate it from the preceding distribution). See the text for details.

(2008): those show a clear predominance of $l = 2$ resonances in direct measurements at $E_{C.M.} \geqslant 1$ MeV.

Angular distribution is analyzed in order to further validate such assumptions: the whole energy range spanned by the experiment is split into three regions ($0 \leqslant E_{C.M.} \leqslant 0.3$ MeV, $0.3 < E_{C.M.} \leqslant 0.6$ MeV, and $0.6 < E_{C.M.} \leqslant 0.9$ MeV), with the aim to have enough statistics in a reasonably small energy interval, where the cross-section can be roughly considered constant.

The yield for the two-body reaction $^{19}F(\alpha, p)^{22}Ne$ reaction is then divided by a Monte Carlo simulation that takes into account the kinematics for the system and the momentum distribution trend. The resulting angular distributions are shown in Figure 9, and the data belonging to the three energy regions are fitted by means of a linear combination of the two spin-parity $J^\pi = 3/2^+$
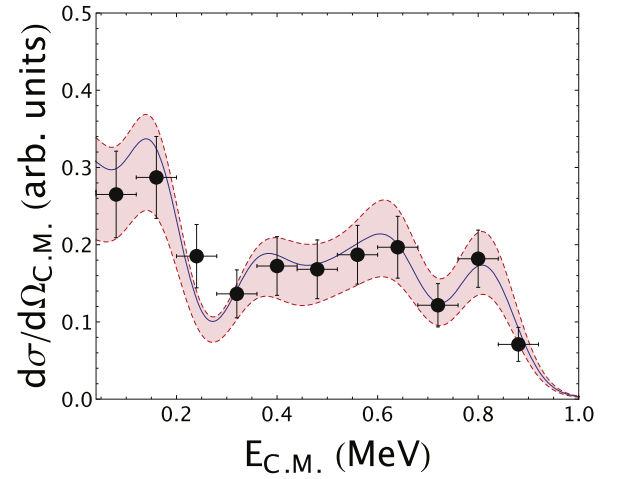

Figure 10. HOES cross-section for the $^{19}F(\alpha, p)^{22}Ne$ reaction. The blue line with the red band represents the *Modified R-matrix* fit along with its error (respectively, see the text for details). All the resonances used for the fit are reported in Table 2.

and $J^\pi = 5/2^+$ angular distributions (Blatt & Biedenharn 1952; La Cognata et al. 2015; see Pizzone et al. 2017 for further details). This combination (shown with red lines in the three panels of Figure 9) is in fair agreement with the experimental errors pointing out a dominant contribution of d-wave for the resonances detected in the region $E_{C.M.} \leqslant 0.9$ MeV. In order to further ascertain the presence of only $l = 2$ resonances, angular distribution for p- and s-waves are also computed, and a poor correspondence with experimental data is found. In particular, p-wave angular distributions are also shown for spin-parity equal to $3/2^-$ and $1/2^-$ (black and green lines in Figure 9, respectively). These distributions clearly do not fit the experimental data.

Moreover, looking at the coefficients for the linear combination of the $J^\pi = 3/2^+$ and $J^\pi = 5/2^+$ fit ($a_{3/2^+}$ and $a_{5/2^+}$ in Figure 9, respectively), the $5/2^+$ contribution strongly dominates over the $3/2^+$ (by seven or nine orders of magnitude).

Once $l = 2$ was ascertained, a fit of the arbitrary unit cross-section using the *Modified R-matrix* method was attempted. We could use the above approach because of the large uncertainties affecting the data: the measurement is therefore not precise enough to allow us to use more sophisticated calculations involving a many-channel approach that takes into account interference. In the calculations, we considered the $l = 2$ levels reported in Pizzone et al. (2017), and the *R-matrix* fit is performed assuming that the proton channel is the dominant one, as pointed out in previous works (Ugalde et al. 2008).

The red band of Figure 10 represents the total error and comes from the uncertainties in the resonance parameters taking into account the statistical error, which is the dominant source of uncertainty: errors on the γ_α parameters are guessed from the *Modified R-matrix* fit simply by matching the upper and lower errors of the experimental points (black dots). The error on the y-axis arises from the statistical uncertainty. Regarding the x-axis, the energy resolution on $E_{C.M.}$ was calculated according to the error propagation starting from experimental errors on energies and angles of the detected particles. The red band of Figure 10 then represents the total error on the fitting procedure made by guessing the upper and lower limit values for γ_p from the *Modified R-matrix* and
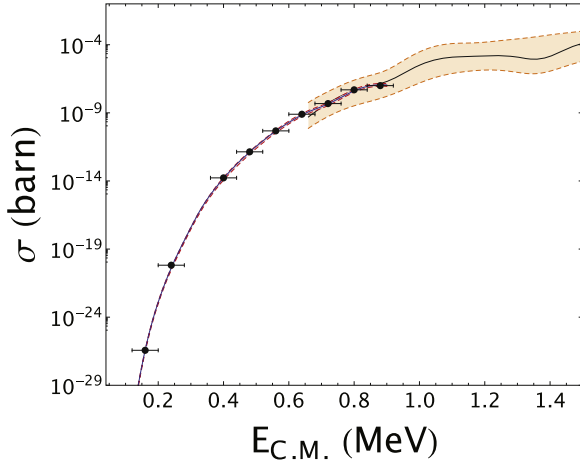
Figure 11. OES cross-section in absolute units (blue line with a red band accounting for uncertainties). The black line with an orange band is the cross-section with its errors coming from direct data, as reported in Ugalde et al. (2008).

matching the upper and lower errors on the ordinate of the experimental points. γ_p and $\gamma_{p'}$ in Table 2 are the reduced widths of the ground and first excited state of the ^{22}Ne particle in the exit channel, respectively.

The fit is also used to evaluate the resonance contribution to the OES ^{19}F(α, p)^{22}Ne: the cross-section $\sigma(E_{C.M.})$, extracted from the HOES one after taking into account the Coulomb and centrifugal barrier penetrability, is determined with the *R-matrix* parameters reported in Table 2 and shown as a blue solid line in Figure 10. Normalizing to direct data of the *R-matrix* fit in the overlapping region between direct measurements and THM data, we are finally able to obtain a cross-section in absolute units.

The result is shown in Figure 11, where the normalization error to the direct data from Ugalde et al. (2008) is also considered (red band), taking into account the average error for the existing measure and then combining it by means of standard error propagation. The black line shows the data available in the literature (Ugalde et al. 2008) along with its error (orange band), both smeared to our experimental resolution (procedure described in La Cognata et al. 2010). It is also important to underline that no direct data below ~660 keV are reported in the literature.

Once the absolute cross-section is obtained, the astrophysical factor $S(E)$ can be calculated. This is important because it removes the Coulomb barrier effects at low energies: the trend in Figure 11 is very steep due to the presence of Coulomb barrier effects. The $S(E)$-factor is reported in a previous work (Pizzone et al. 2017).

6. Reaction Rate

Once the experimental cross-section is extracted, the thermonuclear reaction rate for the ^{19}F(α, p)^{22}Ne reaction is calculated by means of the usual equation:

$$R_{ij} = \frac{N_i N_j}{1 + \delta_{ij}} \langle \sigma \nu \rangle = \frac{N_i N_j}{1 + \delta_{ij}} \left(\frac{8}{\pi A}\right)^{1/2} \left(\frac{1}{k_B T}\right)^{3/2}$$
$$\cdot \int_0^\infty S(E_{C.M.}) \exp\left[-\left(\frac{E_{C.M.}}{k_B T} + 2\pi\eta(E_{C.M.})\right)\right] dE_{C.M.} \quad (5)$$

Table 3
Values of the Constants in Equation (6)

	a	b	c	d
1	1309.18	15.3885	844.952	170.849
2	2568.22	15.7730	16.3666	1.80825
3	520.290	432.940	431.058	37.3312
4	188.174	418.860	634.938	222.838
5	5870.34	12.8279	240.061	13.6220
6	1286.14	36.6741	31.2061	7.37999
7	6374.60	270.212	104.777	88.7584

where σ is the cross-section of the process, ν is the relative velocity of the ij pair of particles, and N_i and N_j are the number of nuclei of the species i and j, respectively.

To correctly evaluate the rate, we parameterized the one published by Ugalde et al. (2008) as follows:

$$R = \exp\left[-a_1 - \frac{a_2}{T_9} - \frac{a_3}{T_9^{1/3}} - a_4 \cdot T_9^{1/3} + a_5 \cdot T_9\right.$$
$$\left. - a_6 \cdot T^{5/3} - a_7 \cdot \mathrm{Log}\, T_9\right] + \exp\left[-b_1 - \frac{b_2 \cdot 10^2}{T_9}\right.$$
$$+ \frac{b_3}{T^{1/3}} - b_4 \cdot T_9^{1/3} + b_5 \cdot T_9 - b_6 \cdot T_9^{5/3}$$
$$\left. + b_7 \cdot \mathrm{Log}\, T_9\right] + \exp\left[-c_1 - \frac{c_2}{T_9} + \frac{c_3}{T_9^{1/3}}\right.$$
$$\left. + c_4 \cdot T_9^{1/3} - c_5 \cdot T_9 + c_6 \cdot T_9^{5/3} + c_7 \cdot \mathrm{Log}\, T_9\right]$$
$$+ \exp\left[d_1 + \frac{d_2}{T_9} + \frac{d_3}{T_9^{1/3}} - d_4 \cdot T_9^{1/3} + d_5 \cdot T_9\right.$$
$$\left. - d_6 \cdot T_9^{5/3} + d_7 \cdot \mathrm{Log}\, T_9\right].$$
$$(6)$$

The values of the a_i, b_i, c_i, and d_i parameters in Equation (6) are reported in Table 3, while T_9 is the temperature in units of 10^9 K.

Using the additivity properties of integrals, the parameterization curve is divided into three regions:

1. $E_{C.M.} \leqslant 0.66$ MeV, where only *R-matrix* theoretical calculations are available (Ugalde et al. 2008);
2. $0.66 < E_{C.M.} \leqslant 0.9$ MeV, obtained by normalization on Hauser–Feshbach calculation at higher energies (Ugalde et al. 2008);
3. $E_{C.M.} > 0.9$ MeV, corresponding to experimental measurements and *R-matrix* fit on data from Ugalde et al. (2008).

The contribution of each part to the integral in Equation (6) is extrapolated from the parameterization and subtracted to the existing reaction rate (Ugalde et al. 2008). Adding the calculation of the new reaction rate performed using the experimental data of the present work, the reaction rate reported in Table 4 is finally obtained.

As reported in the previous work (Pizzone et al. 2017) there is an increase in the contribution of the present channel higher up to a factor of 4 (if upper limits are considered) in the region of astrophysical interest between 0.2×10^9 K and 0.6×10^9 K

Table 4
Values of the Reaction Rate and the Ratio between Experimental THM Results for the Reaction Rate (R_{THM}) Obtained in This Work and the One Parameterized from the Results of Ugalde et al. (2008) (R), $\frac{R_{THM}}{R}$, for Several Temperatures in Units of 10^9 K

Temperature [10^9 K]	$R_{THM} \left[\frac{cm^3}{mol \times sec} \right]$	$\frac{R_{THM}}{R}$
0.10	3.30×10^{-22}	1.37
0.15	3.90×10^{-17}	1.56
0.20	5.97×10^{-14}	1.80
0.25	9.63×10^{-12}	2.58
0.30	4.57×10^{-10}	3.63
0.35	9.43×10^{-09}	3.91
0.40	1.06×10^{-07}	3.15
0.45	7.98×10^{-07}	2.19
0.50	4.67×10^{-06}	1.54
0.60	1.06×10^{-04}	1.04

with respect to the literature (Ugalde et al. 2008). Such an enhancement can be seen in Table 4, along with temperature and rate values. A better refinement of the fitting procedure allows us to narrow the uncertainties and also to find a significant enhancement in the reaction rate in the temperature region $0.1 \times 10^9 \leqslant T \leqslant 0.25 \times 10^9$ K, by a factor of two, with respect to what was reported in Pizzone et al. (2017).

7. Astrophysical Implications

In this section, consequences due to the new rate of the $^{19}F(\alpha, p)^{22}Ne$ reaction are briefly investigated, focusing on the nucleosynthesis of low-mass AGB stars. The fluorine nucleosynthesis in these stars is quite complicated because it involves proton, neutron, and α-captures (Forestini et al. 1992). In particular, ^{19}F production is coupled with slow-neutron-capture processes typical of AGB stars, which leads to the production of about 50% of the nuclei heavier than iron. Indeed, in the He-rich region, during the so-called interpulse period (namely when the H-shell is burning radiatively and the He-burning is quiescent), part of the neutrons released by the $^{13}C(\alpha, n)^{16}O$ are captured and converted into protons by the $^{14}N(n, p)^{14}C$ reaction.

This allows the production of ^{19}F via the chain $^{14}C(\alpha, \gamma)$ $^{18}O(p, \alpha)^{15}N(\alpha, \gamma)^{19}F$ or, alternatively, following $^{14}N(\alpha, \gamma)$ $^{18}F(\beta^+\nu)^{18}O(p, \alpha)^{15}N(\alpha, \gamma)^{19}F$.

Since temperatures are not high enough, the $^{15}N(\alpha, \gamma)^{19}F$ is not activated during the interpulse period, but only when the He-rich materials are engulfed in the thermal pulse (hereafter TP), where He is convectively burned at $T \geqslant 2.5 \times 10^8$ K. In this moment, a further contribution to ^{19}F might come from ^{13}C, if a certain amount remains unburned during the interpulse or is left by the H-burning, which can be engulfed in a TP, leading to the production of ^{15}N and then ^{19}F (Cristallo et al. 2009); this possibility will not be considered in this work. As already mentioned in the Introduction, ^{19}F might also be destroyed by the $^{19}F(p, \alpha)^{16}O$ and $^{19}F(n, \gamma)^{20}F$ reactions. However, the $^{19}F(\alpha, p)^{22}Ne$ during TPs is the main channel for its consumption in low-mass AGB stars, with the abundance of protons in the He-shell being quite poor. In this context, the reaction rate of Table 4 is introduced in the *Software:* NEWTON (Trippella et al. 2014) code for AGB star nucleosynthesis calculation in order to study fluorine production/destruction. In particular, calculations for three stellar models of 1.5, 3, and 5 $M_\odot$ and solar metallicity are performed.

Table 5
Sources of the Reaction Rates Relevant for Fluorine Nucleosynthesis Adopted in Our Calculations

Reaction Rate	Source
$^{13}C(p, \gamma)^{14}N$	Angulo et al. (1999)
$^{13}C(\alpha, n)^{16}O$	Trippella & La Cognata (2017)
$^{14}C(p, \gamma)^{15}N$	Iliadis et al. (2010)
$^{14}C(p, n)^{14}N$	Caughlan & Fowler (1988)
$^{14}C(\alpha, \gamma)^{18}O$	Iliadis et al. (2010)
$^{14}N(p, \gamma)^{15}O$	Adelberger et al. (2011)
$^{14}N(\alpha, \gamma)^{18}F$	Iliadis et al. (2010)
$^{15}N(p, \gamma)^{16}O$	Adelberger et al. (2011)
$^{15}N(p, \alpha)^{12}C$	La Cognata et al. (2007)
$^{15}N(\alpha, \gamma)^{19}F$	Iliadis et al. (2010)
$^{17}O(p, \gamma)^{18}F$	Palmerini et al. (2013)
$^{17}O(p, \alpha)^{14}N$	Sergi et al. (2015)
$^{17}O(\alpha, \gamma)^{21}Ne$	Best et al. (2013a)[a], Angulo et al. (1999)[b]
$^{17}O(\alpha, n)^{20}Ne$	Best et al. (2013a)[a], Angulo et al. (1999)[b]
$^{18}O(p, \gamma)^{19}F$	Adelberger et al. (2011)
$^{18}O(p, \alpha)^{15}N$	La Cognata et al. (2010)
$^{18}O(\alpha, \gamma)^{22}Ne$	Iliadis et al. (2010)
$^{18}O(\alpha, n)^{21}Ne$	Best et al. (2013b)[a], Angulo et al. (1999)[b]
$^{19}F(p, \alpha)^{16}O$	La Cognata et al. (2013)
$^{19}F(p, \gamma)^{20}Ne$	Couture et al. (2008)
$^{19}F(\alpha, p)^{22}Ne$	Ugalde et al. (2008) and this paper

Notes.
[a] For $T_9 \geqslant 0.1$.
[b] For $T_9 < 0.1$.

We adopt the profile for proton injection at the TDU and the resulting budget of ^{13}C and ^{14}N in the He-rich region suggested by Trippella et al. (2016). The same cross-sections for neutron capture reactions used by the quoted authors are also adopted, while the sources for reaction rates of proton and alpha captures are reported in Table 5. Moreover, to better appreciate the effects of the $^{19}F(\alpha, p)^{22}Ne$ reaction rate on ^{19}F nucleosynthesis, other phenomena of ^{19}F destruction due to proton captures, such as the cool bottom process (Palmerini et al. 2011, and references therein) or hot bottom burning (in the case of the 5 $M_\odot$ model, Lattanzio 2003), are supposed to not be at play in our stars.

Figure 12 shows the temporal evolution during the whole TP-AGB phase of the ratio between the ^{19}F abundance obtained in stellar models by adopting the $^{19}F(\alpha, p)^{22}Ne$ reaction rate determined via THM and the one calculated by using the rate published in Ugalde et al. (2008). Blue lines show the ratio of the ^{19}F abundances in the He-rich stellar region after each TP (full dots) and at the end of each interpulse period (open symbols). Taking into account the uncertainties of the THM reaction rate and adopting in the calculation its upper and lower limit, the nucleosynthesis results span the red shaded areas in Figure 12. Panels (a)–(c) deal with AGB models of 1.5, 3, and 5 $M_\odot$, respectively. As reported in Table 4, at the typical temperature of the He-shell burning (a few 10^8 K), the rate of the $^{19}F(\alpha, p)^{22}Ne$ reaction determined by the THM experiment is always larger than the one measured by Ugalde et al. (2008); as a consequence, the ^{19}F is more easily destroyed during TP and the abundances predicted for the stellar interior are smaller. The 5 $M_\odot$ AGB model (panel (c)) is the most sensitive to the $^{19}F(\alpha, p)^{22}Ne$ reaction rate used in our calculations. Indeed, the ^{19}F abundance in the He-shell is reduced down to a factor of 4 in the last pulses because the temperature reaches
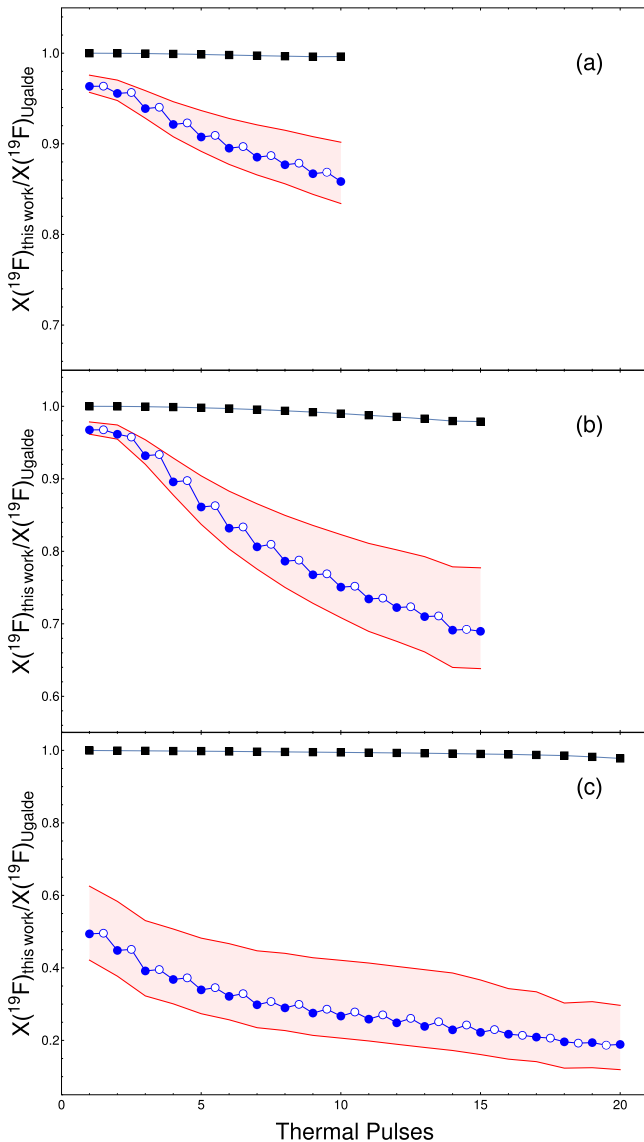
Figure 12. Temporal evolution of the ratio between the ^{19}F abundance obtained in AGB models by adopting a ^{19}F$(\alpha, p)^{22}$Ne reaction rate and the ones obtained by using the rate published by Ugalde et al. (2008). In abscissa the number of thermal pulses that follow through the whole AGB phase are reported. In this notation, the time increases from left to right. Panels (a)–(c) deal with AGB models of solar metallicity with masses of 1.5, 3, and 5 $M_\odot$, respectively. Black lines represent the evolution of the ^{19}F surface abundance for each AGB model, and solid black points indicate the surface composition after each TP and the subsequent TDU. Blue lines show the ratio of the ^{19}F abundance in the He-rich stellar region at the end of each TP (full dots) and before the on-set of the subsequent He-burning episode at the end of the interpulse periods (open symbols). Red shaded areas show the spread of nucleosynthesis code results by adopting in calculations the upper and the lower limit of the ^{19}F$(\alpha, p)^{22}$Ne reaction rate presented in this paper.

3.6×10^8 K that corresponds to the energy at which the difference between the THM cross-section and the Ugalde et al. (2008) one is maximum. Variations are smaller in the 1.5 $M_\odot$ and the 3 $M_\odot$ models, whose He-shell burning temperatures do not exceed 2.9 and 3.2×10^8 K, respectively. Once the ashes of the He-burning are brought into stellar surface by TDU, the nucleosynthesis products are diluted with envelope materials and the effects of the ^{19}F$(\alpha, p)^{22}$Ne reaction rate become negligible. This is pointed out by the black curves in the three panels of Figure 12, which show the temporal evolution of the

ratio of the surface ^{19}F abundance of the models computed by using the THM reaction rate and of the ones obtained with the ^{19}F$(\alpha, p)^{22}$Ne rate from Ugalde et al. (2008). None of the studied cases shows a variation in the ratio larger than 5%. Since the cross-section of the ^{19}F$(\alpha, p)^{22}$Ne reaction measured through the THM is up to a factor of 4 larger than that reported in the literature (Ugalde et al. 2008), we believe that this experimental results could crucially affect our knowledge of ^{19}F nucleosythesis in the most relevant energy region for He-shell burning. Such an analysis will be the subject of a forthcoming paper.

8. Conclusions

A new measurement for the ^{19}F$(\alpha, p)^{22}$Ne reaction was performed using the THM, by means of the three-body process ^{6}Li$(^{19}$F, p^{22}Ne$)d$. In this work, the cross-section (in absolute units) and the reaction rate were evaluated, along with the impact of the measurement on the astrophysical scenario of AGB-star nucleosynthesis. For the first time, the experimental cross-section was measured covering the whole Gamow window and the contribution of several resonances in the energy range of interest for astrophysics is outlined. We also found that the ^{19}F$(\alpha, p)^{22}$Ne reaction rate, measured through the THM and presented in this paper, when adopted in AGB star models might account for a ^{19}F destruction via He-burning up to 5 times more efficient than what has been estimated so far by using other data in the literature (Ugalde et al. 2008). Nevertheless, the temporal evolution of the superficial abundance of ^{19}F did not show a variation larger than 5% with respect to the calculation made with the data from Ugalde et al. (2008) in the stellar envelope.

ORCID iDs

G. D'Agata ⬤ https://orcid.org/0000-0001-5261-8329
R. G. Pizzone ⬤ https://orcid.org/0000-0003-2436-6640
M. La Cognata ⬤ https://orcid.org/0000-0002-1819-4814
C. Spitaleri ⬤ https://orcid.org/0000-0001-6256-9727
S. Palmerini ⬤ https://orcid.org/0000-0001-5386-8389
O. Trippella ⬤ https://orcid.org/0000-0002-4757-0487
D. Vescovi ⬤ https://orcid.org/0000-0003-0309-4666
S. Cherubini ⬤ https://orcid.org/0000-0002-1974-0389
P. Figuera ⬤ https://orcid.org/0000-0003-2321-2463
M. Gulino ⬤ https://orcid.org/0000-0003-4125-9150
R. Kshetri ⬤ https://orcid.org/0000-0002-4456-0507
L. Lamia ⬤ https://orcid.org/0000-0002-4055-0811
M. Lattuada ⬤ https://orcid.org/0000-0003-3907-9230
M. Milin ⬤ https://orcid.org/0000-0002-4375-5951
G. G. Rapisarda ⬤ https://orcid.org/0000-0003-4064-2609
M. L. Sergi ⬤ https://orcid.org/0000-0002-6631-0015
A. Tumino ⬤ https://orcid.org/0000-0002-6953-7725

References

Abia, C., Cunha, K., Cristallo, S., et al. 2010, ApJL, 715, L94
Abia, C., Cunha, K., Cristallo, S., et al. 2015, A&A, 581, A88
Abia, C., Recio-Blanco, A., de Laverny, P., et al. 2009, ApJ, 694, 971
Adelberger, E. G., García, A., Robertson, R. G. H., et al. 2011, RvMP, 83, 195
Alves-Brito, A., Karakas, A. I., Yong, D., et al. 2011, A&A, 536, A40

Angulo, C., Arnould, M., Rayet, M., et al. 1999, NuPhA, 656, 3
Assenbaum, H., Langanke, K., & Rolfs, C. 1987, ZPhyA, 327, 461
Barbarino, S., Lattuada, M., Riggi, F., et al. 1980, PhRvC, 21, 1104
Best, A., Beard, M., Görres, J., et al. 2013a, PhRvC, 87, 045805
Best, A., Falahat, S., Görres, J., et al. 2013b, PhRvC, 87, 045806
Blatt, J. M., & Biedenharn, L. C. 1952, RvMP, 24, 258
Caughlan, G. R., & Fowler, W. A. 1988, ADNDT, 40, 283
Cherubini, S., Gulino, M., Spitaleri, C., et al. 2015, PhRvC, 92, 015805
Couture, A., Beard, M., Couder, M., et al. 2008, PhRvC, 77, 1
Cristallo, S., Di Leva, A., Imbriani, G., et al. 2014, A&A, 570, 46
Cristallo, S., Straniero, O., Gallino, R., et al. 2009, ApJ, 696, 797
Dolinsky, E. I., Dzhamalov, P. O., & Mukhamedzhanov, A. M. 1973, NuPhA, 202, 97
Forestini, M., Goriely, S., Jorissen, A., & Arnould, M. 1992, A&A, 261, 157
Goriely, S. E., Jorrissen, A., & Arnould, M. 1989, in Proc. 5th Workshop on Nuclear Astrophysics, MPA/P1, ed. W. Hillebrandt & E. Muller, 60
Gulino, M., Spitaleri, C., Tang, X., et al. 2013, PhRvC, 87, 12801
Iliadis, C., Longland, R., Champagne, A. E., et al. 2010, NuPhA, 841, 31
Indelicato, I., La Cognata, M., Spitaleri, C., et al. 2017, ApJ, 845, 19
Jönsson, H., Ryde, N., Harper, G. M., et al. 2014, ApJL, 789, L41
Jönsson, H., Ryde, N., Spitoni, E., et al. 2017, ApJ, 835, 50
Jorissen, A., Smith, V. V., & Lambert, D. L. 1992, A&A, 261, 164
Keyworth, G. A., Wilhjelm, P., Kyker, G. C., et al. 1968, PhRv, 176, 1302
Kobayashi, C., Izutani, N., Karakas, A. I., et al. 2011, ApJL, 739, L57
La Cognata, M., Mukhamezhanov, A., Spitaleri, C., et al. 2011, ApJL, 739, L54
La Cognata, M., Palmerini, S., Spitaleri, C., et al. 2015, ApJ, 805, 128
La Cognata, M., Romano, S., Spitaleri, C., et al. 2007, PhRvC, 76, 065804
La Cognata, M., Spitaleri, C., & Mukhamezhanov, A. 2010, ApJ, 723, 1512
La Cognata, M., Spitaleri, C., Trippella, O., et al. 2013, ApJ, 777, 143
Lamia, L., Spitaleri, C., Pizzone, R. G., et al. 2013, ApJ, 768, 65
Lane, A. M., & Thomas, R. G. 1958, RvMP, 30, 257
Lattanzio, J. 2003, in IAU Symp. 209, Planetary Nebulae: Their Evolution and Role in the Universe, ed. S. Kwok, M. Dopita, & R. Sutherland (San Francisco, CA: ASP), 73
Longland, R., Lorén-Aguilar, P., José, J., et al. 2011, ApJL, 737, L34
Lucatello, S., Masseron, T., Johnson, J., et al. 2011, ApJ, 729, 40

Lugaro, M., Ugalde, C., Karakas, A. I., et al. 2004, ApJ, 615, 934
Mahaux, C., & Weidenmüller, H. A. 1969, Shell-Model Approach to Nuclear Reactions (Amsterdam: North-Holland)
Meynet, G., & Arnould, M. 2000, A&A, 355, 176
Mukhamedzhanov, A. M., Blokhintsev, L. D., Irgaziev, B. F., et al. 2008, JPhG, 35, 014016
Mukhamedzhanov, A. M., Shubhchintak, & Bertulani, C. A. 2017, PhRvC, 96, 024623
Palacios, A., Arnould, M., & Meynet, G. 2005, A&A, 443, 243
Palmerini, S., La Cognata, M., Cristallo, S., & Busso, M. 2011, ApJ, 729, 3
Palmerini, S., Sergi, M. L., La Cognata, M., et al. 2013, ApJ, 764, 128
Pilachowski, C. A., & Pace, C. 2015, AJ, 150, 66
Pizzone, R. G., D'Agata, G., La Cognata, M., et al. 2017, ApJ, 836, 57
Pizzone, R. G., Mukhamezhanov, A., Spitaleri, C., et al. 2009, PhRvC, 80, 025807
Pizzone, R. G., Roeder, B., McKluskey, M., et al. 2016, EPJA, 52, 24
Pizzone, R. G., Spartá, R., Bertulani, C., et al. 2014, ApJ, 786, 112
Pizzone, R. G., Spitaleri, C., Cherubini, S., et al. 2005, PhRvC, 71, 058801
Schuler, S. C., Cunha, K., Smith, V. V., et al. 2007, ApJL, 667, L81
Sergi, M. L., Spitaleri, C., La Cognata, M., et al. 2015, PhRvC, 91, 065803
Spitaleri, C., La Cognata, M., Lamia, L., et al. 2016, EPJA, 52, 77
Spitaleri, C., Lamia, L., Tumino, A., et al. 2004, PhRvC, 69, 055806
Spitaleri, C., Typel, S., Pizzone, R. G., et al. 2001, PhRvC, 63, 055801
Spitaleri, C. 1991, in Problems of Fundamental Modern Physics, II: Proceedings, ed. R. Cherubini, P. Dalpiaz, & B. Minetti (Singapore: World Scientific), 21
Thielemann, F. K., Arnould, M., & Truran, J. W. 1986, MPARp, 15, 262
Tribble, R. E., Bertulani, C., La Cognata, M., et al. 2014, RPPh, 77, 106901
Trippella, O., Busso, M., Maiorca, E., et al. 2014, ApJ, 787, 41
Trippella, O., Busso, M., Palmerini, S., et al. 2016, ApJ, 818, 125
Trippella, O., & La Cognata, M. 2017, ApJ, 837, 41
Tumino, A., Spartá, R., Spitaleri, C., et al. 2014, ApJ, 785, 96
Tumino, A., Spitaleri, C., Mukhamedzhanov, A. M., et al. 2011, PhLB, 700, 111
Ugalde, C., Azuma, R. E., Couture, A., et al. 2008, PhRvC, 77, 035801
Woosley, S. E., & Haxton, W. C. 1988, Natur, 334, 45